

Supplementary Materials

Protein and Lipid Mass Concentration Measurement in Tissues by Stimulated Raman Scattering Microscopy

Seungeun Oh^{1a}, ChangHee Lee^{2a}, Wenlong Yang^{3,4}, Ang Li^{1,3}, Avik Mukherjee¹, Markus Basan¹, Chongzhao Ran⁵, Wei Yin⁵, Clifford J. Tabin², Dan Fu^{3,6*}, X. Sunney Xie^{3,7}, Marc W. Kirschner^{1*}

¹Harvard Medical School, Department of Systems Biology, 200 Longwood Avenue, Boston, MA 02115, USA

²Harvard Medical School, Department of Genetics, 77 Avenue Louis Pasteur, Boston, MA 02115, USA

³Department of Chemistry and Chemical Biology, Harvard University, Cambridge, MA 02138, USA

⁴Center for Advanced Imaging, Harvard University, Cambridge, MA 20138, USA

⁵Athinoula A. Martinos Center for Biomedical Imaging, Massachusetts General Hospital and Harvard Medical School, Boston, MA 02129, USA

⁶University of Washington, Department of Chemistry, Seattle, WA 98195 USA

⁷Beijing Advanced Innovation Center for Genomics, Peking University, Beijing, China and Biomedical Pioneering Innovation Center, Peking University, Beijing, China

^a Co-first authors

* Corresponding authors: marc@hms.harvard.edu, danfu@uw.edu

Table of Contents

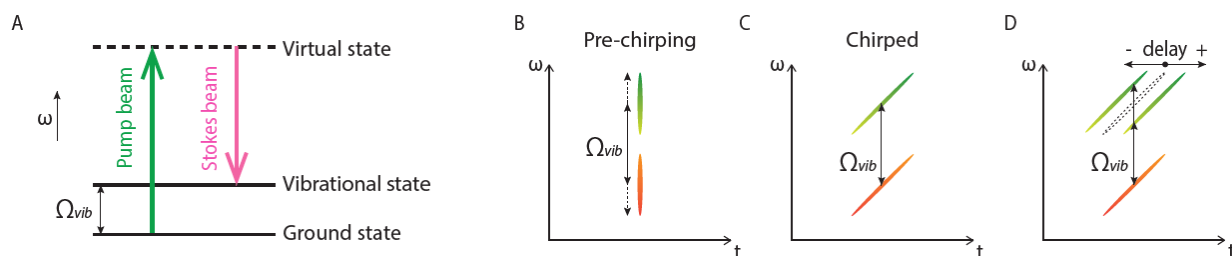
1. Supplementary methods	2
1.1. Supplementary method for the spectral-focusing stimulated Raman scattering microscope	2
1.2. Image acquisition and resolution	5
1.3. Pre-processing of SRS images	5
1.4. Protocol for making calibration standards	6
1.5. Protocol for measuring SRS intensity of the calibration standards	6
1.6. Computation of the decomposition matrix.....	7
1.7. Applying the decomposition matrix to sample data	8
1.8. Demonstration of NoRI measurements	9
1.9. Simultaneous fluorescence imaging with NoRI.....	10
2. Cell culture sample preparation	11
3. Animal protocols	12
4. Tissue sample preparation	12
5. Tomographic phase microscopy imaging protocol.....	12
6. Image segmentation methods	13
6.1. Image segmentation based on protein and lipid concentrations.....	13
6.2. Image segmentation of brain tissue NoRI images	14
7. Statistics	15
8. Supplementary theory of NoRI	15
9. Wavelength dependence of light scattering: impact on imaging depth limit	16
10. Depth dependence of the measurement sensitivity of the concentration	16
11. Limitations of the absolute concentration measurement by NoRI	18
11.1. Chemical components of sample	18
11.2. Calibration reference materials	19
11.3. Pigmented samples	20
12. Supplementary figures.....	21
13. Supplementary references.....	24

1. Supplementary methods

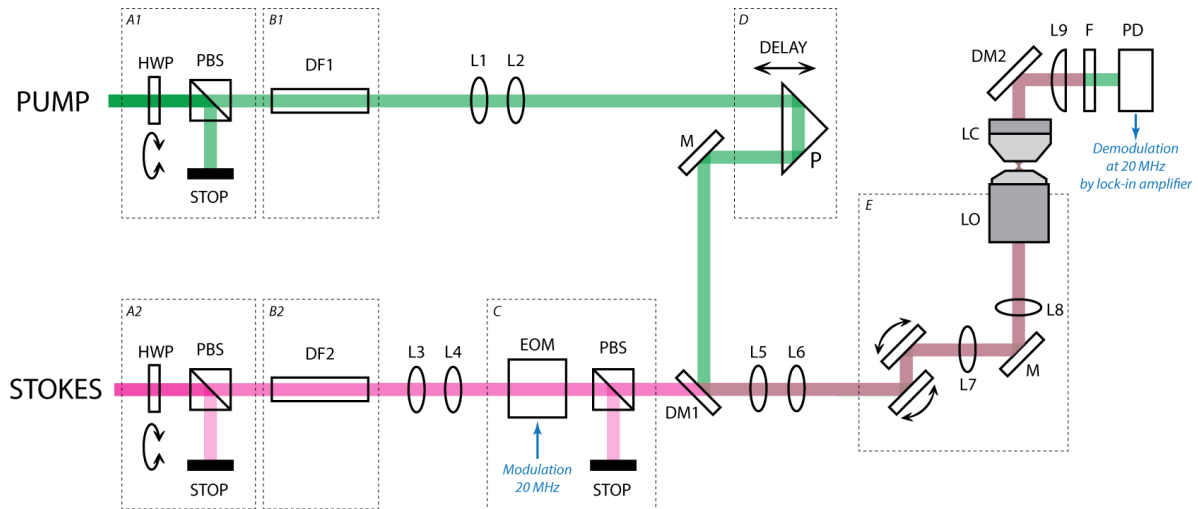
1.1. Supplementary method for the spectral-focusing stimulated Raman scattering microscope

NoRI is based on SRS microscopy of the high wavenumber Raman bands in range of 2853-3420 cm^{-1} . These Raman peaks are broad and have strong intensity and can be easily detected by many types of SRS microscope. However, not all SRS microscopes are suitable since the application of the NoRI algorithm requires that the intensity difference between different Raman bands are consistent throughout calibration and sample imaging. Use of high-stability optomechanical components, ambient temperature regulation, and encasing the free space optical components with enclosure improves repeatability. The optical system needs to be fully automated to eliminate manual optical adjustments that can introduce irreproducibility between calibration and sample imaging. The most crucial element for repeatability is the light source. Tunable picosecond pulse lasers were the original choice of light source, since they have the advantage of straightforward Raman band selection¹. But wavelength tuning to cover the 2853-3420 cm^{-1} band requires temperature changes which often require manual adjustment of the OPO cavity and Lyot filter. We found that femtosecond pulse laser (Spectra-Physics, Insight X3) lacks manual adjustment and provides sufficient repeatability (Supplementary Fig. 1). It can be combined with spectral-focusing to achieve comparable spectral resolution as picosecond pulse lasers. Therefore, we built a custom SRS microscope comprised of a tunable femtosecond pulse laser and dense flint dispersion element for spectral-focusing (Fig.1a, Supplementary Fig. 2)².

Supplementary Fig. 2 illustrates the optical layout of the microscope. It includes a dual-output tunable femtosecond laser, dispersion elements for spectral focusing, electro-optic amplitude modulation for lock in amplification, a motorized delay for spectrum selection, a point-scanning microscope, a detector for measuring stimulated Raman loss and a lock-in amplifier. The dual-output tunable femtosecond laser (Spectra-Physics, Insight X3) provides a tunable beam (680-1040 nm) and a fixed wavelength beam (1045 nm), which are used as the pump beam and the Stokes beam, respectively. The tunable wavelength pump beam allows selection of Raman bands as depicted in Supplementary Fig. 1A. The laser power is reduced by a pair of attenuators consisting of motor controlled half wave plates and cube polarizers (Supplementary Fig. 2 A1, A2). After power attenuation, the pump beam power and the Stokes beam power at the sample were 52–88 mW and 25-39 mW, respectively. For enhanced long-term stability, beam height was reduced to 2 inches (50.8 mm) from the optical table by a periscope (not shown), and most optical components were glued to kinematic mounts affixed on 1-1.5 inch diameter optical posts made or directly mounted to the optical table. Optomechanics components made with heat-treated stainless steel with low coefficient of thermal expansion (Thorlabs, Polaris optomechanics) were used for mirror mounts, posts and post clamping arms. The pump beam and the Stokes beam are chirped by passing 4 times through high dispersion dense flint glass rods of 130 mm and 150 mm lengths, respectively (Supplementary Fig. 2 B1, B2; Casix, SF57). This chirping enhances spectral resolution and



Supplementary Figure 1. Principle of spectral focusing in stimulated Raman scattering imaging. (A) The stimulated Raman scattering process is selective for the vibrational mode whose energy Ω_{vib} matches the energy difference between the pump beam and the Stokes beam. (B) Femtosecond pulses have a broad bandwidth, resulting in reduced resolution in vibrational spectrum. (C) Chirped pulses have narrow instantaneous bandwidth and enhances the spectral resolution. (D) The energy difference between the pump beam and the Stokes beam can be adjusted by changing the temporal overlap of the two chirped pulses. This is adjusted by a controllable delay in the optical path of the pump beam.



Supplementary Figure 2. Schematics of spectral focusing SRS microscope optics. PUMP, tunable output of the femtosecond laser; STOKES, 1045 nm output of the femtosecond laser; (A1, A2) Power attenuation modules. HWP, half waveplate; PBS, polarizing beam splitter; STOP, beam stop; (B1, B2) Pulse chirping for spectral focusing. DF1-2, SF57 glass rods; (C) Power modulation module for lock-in amplification. EOM, electro-optic modulator; (D) Motorized delay for spectrum selection and scanning. P, retroreflector prism; (E) A confocal laser scanning microscope; PD, photo diode; DM1-2, dichroic mirrors; M, mirror; L1-6, relay lens pairs for adjusting the beam diameter; L7, scan lens; L8, tube lens; LO, objective lens, LC, condenser lens.

is referred to as spectral focusing (Supplementary Fig. 1B and 1C). The amplitude of the Stokes beam is modulated by a resonant electro-optic modulator (Supplementary Fig. 2 EOM; Thorlabs EO-AM-R-20-C2) at 20 MHz (Supplementary Fig. 2 C). To drive the EOM, the sinusoidal output from a function generator internal to the lock-in amplifier (Zurich Instruments, UHFLI) is amplified by using a RF power amplifier (Mini-Circuits, ZHL-1-2W). The modulation depth is maximized by adjusting the amplitude of the driving voltage. A motor-controlled retroreflector prism controls the optical path length of the pump beam (Supplementary Fig. 2 D). This path length adjustment provides a fine control of spectrum selection (Supplementary Fig. 1D)². The Stokes beam is combined with the pump beam using a dichroic mirror (Supplementary Fig. 2 DM1; Semrock, LP02-980RE-25). Path length of the pump beam path prior to the dichroic mirror is appropriately adjusted to ensure temporal overlap of the pump pulse and the Stokes pulse after the dichroic mirror. The pulse overlap can be determined at the resolution of nanoseconds (equivalent to millimeter distance of path length) using a pair of high speed photo detectors (Thorlabs, DET10A) and a high bandwidth oscilloscope (≥ 500 MHz). Finer adjustment of the pulse overlap is made by the motorized delay using the SRS signal from a sample. The combined beams enter a laser scanning microscope (Supplementary Fig. 2 E; Olympus, FV3000) to image the sample by point scanning. Sample is placed between a water immersion 60x 1.2NA objective lens (Supplementary Fig. 2 LO, Olympus, UPLSAPO60XWIR) and oil immersion 1.4 NA condenser (Supplementary Fig. 2 LC, Nikon, D-CUO Achr-Apl NA=1.40). The sample space is 1.83 mm when the condenser is directly immersed in the culture dish (without immersion oil) and 0.63 mm when imaging through 1.2 mm thick slide glass (with immersion oil). The transmitted light is collected by the condenser lens and focused on a high speed photodiode (Supplementary Fig. 2 PD; Thorlabs, FDS1010) located on the trans-side of the sample using a focusing lens (Supplementary Fig. 2 L9). The light path is folded by 90 degrees using a dichroic mirror (Supplementary Fig. 2 DM2; Edmund Optics, 69-218) to allow transillumination for bright field viewing of the sample through microscope eyepiece. The Stokes beam is rejected before the detector with an IR filter (Supplementary Fig. 2 F; Edmund Optics, 54-517) and stimulated Raman loss of the pump beam is measured. Bias voltage of 70 V was applied to the photodiode. The photo current is converted to voltage with a 50Ω resistor, filtered by a 3–30 MHz bandpass filter (Mini-Circuits, ZABP-16+), and demodulated by a lock-

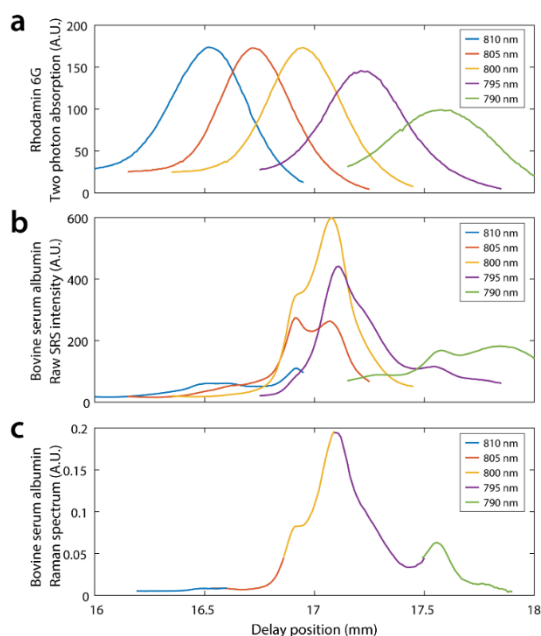
in amplifier (Zurich Instruments, UHFLI) at the EOM modulation frequency. The demodulation amplitude from the lock-in amplifier is registered to images in real time by an analog-to-digital data acquisition board (Olympus, Analog Box) synchronized to the scanning of the microscope.

The tunable laser wavelength and delay position parameters for the CH₃, CH₂, H₂O and other desired Raman bands are determined as follows. The pump beam wavelength for selecting a Raman band of vibrational energy Ω_{vib} is determined by $\Omega_{vib} = 1/\lambda_p - 1/\lambda_s$, where λ_p and λ_s are the wavelengths of pump beam and Stokes beam, respectively (Supplementary Fig. 1A). Supplementary Table 1 shows the pump beam wavelengths for the CH₃, CH₂, H₂O and nucleic acids Raman bands. Once the pump beam wavelength is set, as described above, we determine the delay position for the CH₃, CH₂, and H₂O Raman peaks. For this, we acquire spectral scans of pure samples (BSA, DOPC, water, or DNA) by scanning the delay motor at the respective pump beam wavelength shown in Supplementary Table 1. The measured SRS spectrum is the convolution of the Raman spectrum and the overlap of chirped pump and Stokes pulses (Fig. 1b)². The pulse overlap is a function of the delay position can be measured from two-photon absorption (TPA) of Rhodamine 6G solution (Supplementary Fig. 3a). Raw SRS intensity is divided by Rhodamine 6G TPA to obtain the Raman spectrum (Supplementary Fig. 3c).

For routine imaging, the delay position at the peak of CH₃, CH₂, and H₂O peaks were saved in preset files. Since the linear delay motor position and Raman spectrum wavenumber are linearly related², the delay position can be mapped to wavenumbers by linear fitting using the CH₂ and CH₃ Raman peaks. We wrote Matlab scripts to automate SRS image acquisition at the Raman bands. Matlab preset files stored the parameters of wavelength, delay position, and power attenuation for respective Raman bands. The setting of the scanning microscope such as the scan positions, z-scan range, and scan resolution were controlled from Olympus Fluoview, which in turn was controlled by Matlab via the Remote Development Kit (Olympus, RDK) library.

Supplementary Table 1. Pump beam wavelengths for selected Raman bands

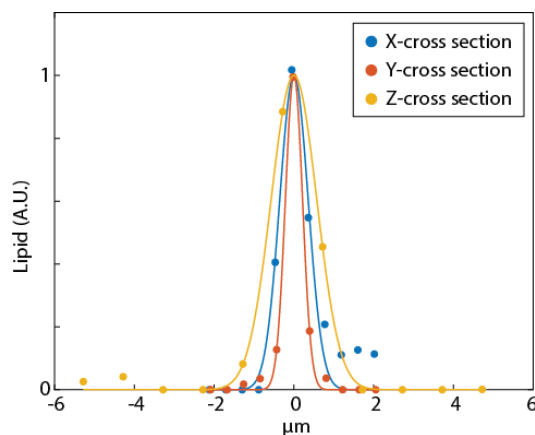
Raman band	Ω_{vib} (cm ⁻¹)	Stokes beam wavelength (nm)	Pump beam wavelength (nm)
CH ₃	2935	1045	800
CH ₂	2853	1045	805
H ₂ O	3420	1045	770
Nucleic acids	2967	1045	796



Supplementary Figure 3. Raman spectrum measurements using the spectral-focusing SRS microscope. A spectrum is acquired by scanning the delay length of the pump beam. (a) Pulse overlap of pump beam and Stokes beam is measured from two photon absorption of Rhodamine 6G dissolved in deuterated water. Colors indicate different pump beam wavelengths as per legend. The Stokes beam wavelength is 1045nm. (b) Raw SRS intensity of bovine serum albumin as a function of pump beam delay at respective pump beam wavelengths. (c) By dividing (b) with (a) after dark signal subtraction, the Raman spectrum of bovine serum albumin is obtained. Data is truncated at the edges of each scan where noise is large due to the low two photo absorption signal.

1.2. Image acquisition and resolution

All SRS images are acquired with 2 microsecond per pixel dwell time. As such, the acquisition time for a single 512x512 resolution SRS image is about 1 second. In a typical NoRI measurement, three Raman bands are acquired at 2853, 2935, and 3250 cm^{-1} . A Raman band change requires a wavelength change of the tunable laser, which takes 7–11 seconds to finish and limits the rate of time series data acquisition. When scanning a large sample area of a fixed sample, we imaged the entire sample area at each Raman band to minimize the time for switching the pump beam wavelength. In these cases, we minimized image misalignment between different Raman bands by clamping the sample to the stage and equilibrating it with the environmental temperature before scanning. At the 60x magnification, the field of view is approximately 212 μm x 212 μm . Therefore, the time to image a 1 cm x 1 cm area at a single z plane is about 2 hours. Frame averaging of 4 to 16 frames were used in 4-component NoRI imaging for nucleic acid concentration measurement (Supplementary Fig. 15). No frame averaging was used in other cases unless noted. Theoretical resolution at 60x magnification was 0.34 μm laterally and 0.85 μm axially³ (0.57 μm and 1.58 μm when converted to full-width-half-maximum⁴). To demonstrate the practical resolution in tissue imaging, we measured a lipid droplet located at 44 μm depth inside a 100 μm thick section of cartilage tissue without frame averaging (Supplementary Fig. 4). Full-width-half-maximum of the lipid droplet was 1.18 μm and 0.714 μm in x and y and 1.90 μm in z, which is slightly larger than the theoretical resolution.



Supplementary Figure 4. Cross section of a small lipid droplet.

1.3. Pre-processing of SRS images

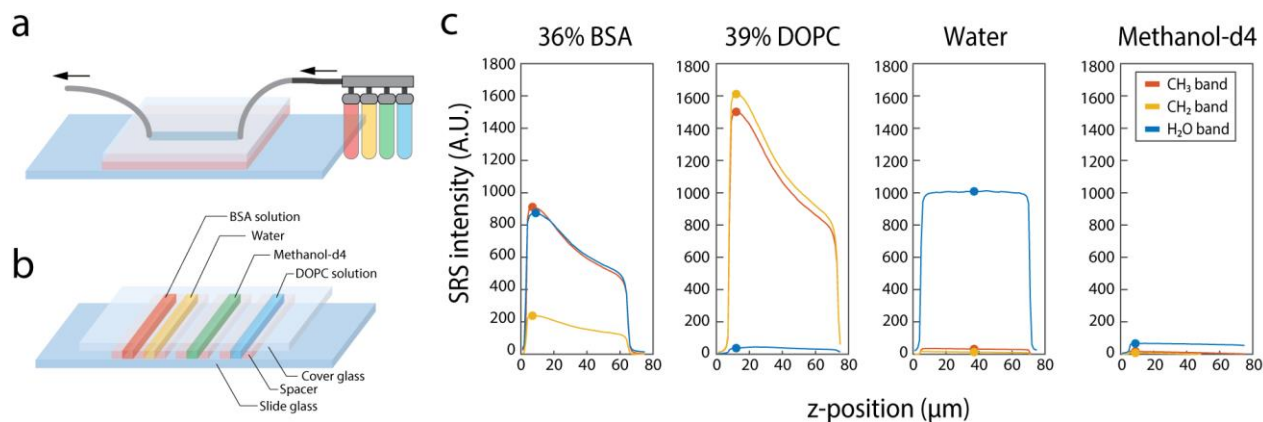
To ensure the linearity of the SRS intensity in the entire signal range including small signals near zero, in-phase amplitude (X) is chosen for lock-in amplifier output and a small constant offset is added to the output. The offset is subtracted after analog to digital conversion by subtracting the background level measured when the light is blocked. After the background subtraction (which is same for all Raman bands), SRS images were divided by the flat field correction mask of the matching Raman band. This is necessary because the SRS intensity is stronger at the center of the field of view than in the periphery due to aberrations of the optical system. This spatial variation of intensity does not change with time or repeated changing of the pump beam wavelength, but are different for different pump wavelengths. Flat-field correction masks were created by measuring the intensity profile of BSA solution at 770 nm, 796 nm, and 800 nm pump wavelengths (for the H_2O , nucleic acids, and CH_3 Raman bands respectively) and from DOPC solution at 805 nm pump wavelength (for the CH_2 Raman band). An SRS intensity image at the z plane of the highest intensity is smoothed by 2D polynomial fitting⁵ and normalized by dividing with the maximum intensity. The mask is generated from a single z plane of the calibration samples but applied to all z planes in the sample data.

1.4. Protocol for making calibration standards

Calibration standards consist of bovine serum albumin (BSA) solutions in water, dioleoyl-phosphocholine (DOPC) solutions in 4-deuterated methanol, pure water and pure 4-deuterated methanol. All solution samples were mixed by measuring the weights of the components. BSA powder (Sigma Aldrich, A7638) was weighed in a conical tube and 150 mM pH7.6 phosphate buffer was added to make the concentration of 30-33% (w/w). The tube is tightly closed and placed in a shaker at 40 °C until BSA is fully dissolved, while occasionally spinning down undissolved chunks stuck on the tube wall. DOPC powder (Avanti Polar Lipids, 850375) was weighed in a conical tube, to which 4-deuterated methanol (Sigma-Aldrich, 151947) was added to a final concentration of 15-39%. A double strand DNA solution was used in the 4-component NoRI (Supplementary Fig. 15). Double stranded DNA powder from salmon testes (Calbiochem, 262012) was weighted in a conical tube and water was added to make the final concentration 5% (w/v). The tube was tightly closed and placed in a shaker at 37 °C overnight until all the DNA was dissolved. The final concentration in volume fraction was calculated from the mass fractions and the density of the pure components, which is 1.364 g/ml for BSA⁶, 1.01 g/ml for DOPC⁷, and 1.7 g/ml for DNA⁸.

1.5. Protocol for measuring SRS intensity of the calibration standards

To compute the decomposition matrix, calibration standard samples need to be imaged under the same imaging conditions. This can be achieved by flowing different sample solutions into a single same imaging chamber, but this method requires that the fluidics system is flushed between samples and large quantity of standard solution is consumed in the process (Supplementary Fig. 5a). We find it convenient to assemble all calibration standard samples on a glass slide by creating multiple sample holding slots using adhesive sheets (Grace Biolabs, SA-S-1L)(Supplementary Fig. 5b). The slots were created with regular spacing using a laser cutter to automate the image acquisition. The size of the sample holding slot was 2 mm width, 24 mm length, and 120 μm thickness and held about 6 μl of solution. To prevent mixing of the adjacent samples, we added empty slots around the DOPC sample and the d-methanol sample. The samples were injected using a micropipette and sealed with vacuum grease. Supplementary Fig. 5c shows SRS intensity z-profiles of each sample measured at the CH_3 , CH_2 and H_2O Raman bands. The SRS intensity of the water sample is independent of the z position, as the objective lens is corrected for water. But the intensity of BSA and DOPC samples is strongest at the surface immediately past the cover glass and decreases with increasing z-depth as the focus degrades as light pass through the index-mismatched solutions. 4-deuterated methanol used as the solvent for DOPC has practically zero signal in all three Raman bands. For the computation of the spectral decomposition matrix, the average SRS intensity values are measured at the z plane of highest intensity for protein and lipid, and at the mid-z-plane for water and 4-

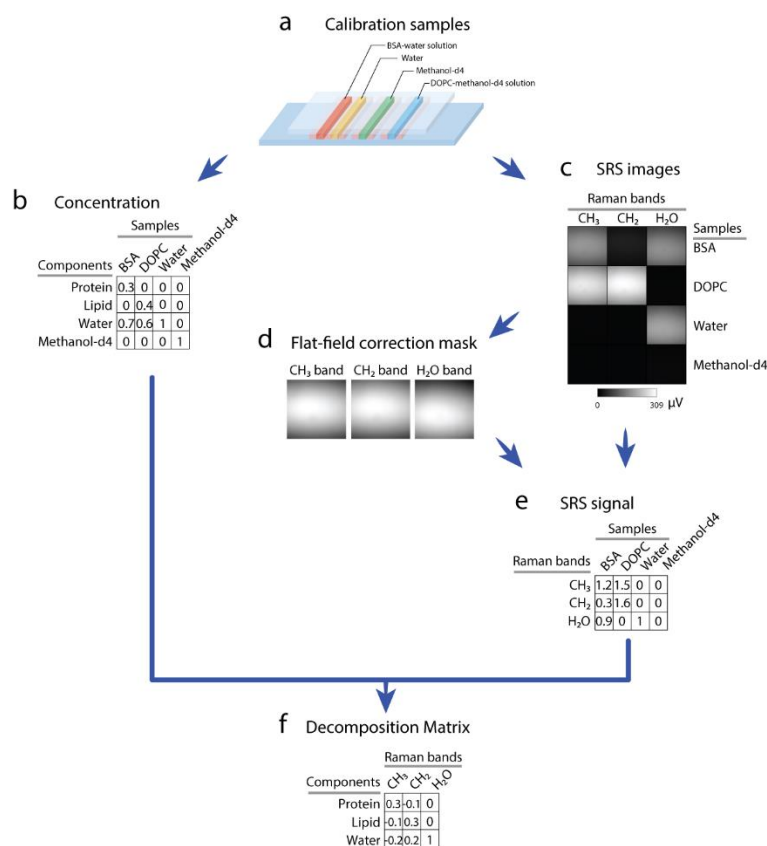


Supplementary Figure 5. (a) Flow channel for measuring calibration samples under an identical imaging condition. (b) Multi-channel slide assembly for calibration samples. (c) Z-profiles of SRS intensity of calibration standard samples. Filled circles mark where the SRS signal intensity is taken for the calculation of the decomposition matrix.

deuterated methanol. This measurement was performed after background-subtraction and flat-field-correction of the raw SRS intensity images.

1.6. Computation of the decomposition matrix

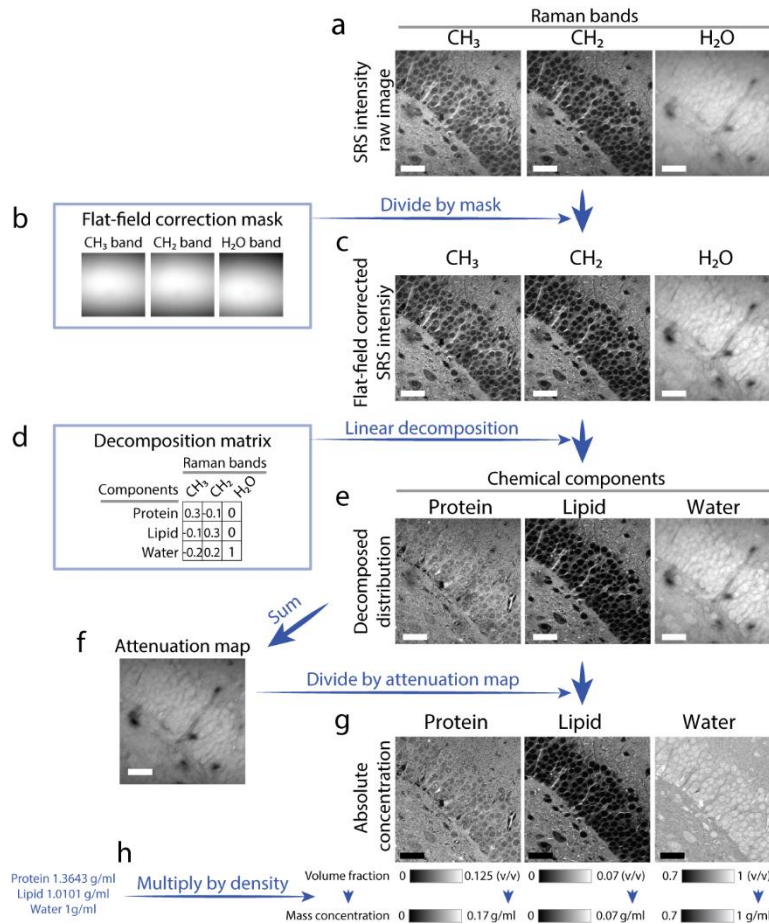
We obtained the spectral decomposition matrix that maps S , the SRS intensities of the calibration samples at the CH_3 , CH_2 , and H_2O Raman bands, to C , the protein, lipid, and water concentration of the calibration samples in the following manner. The matrix S is defined as a 3×4 matrix where S_{ik} denotes SRS intensities of the BSA standard solution, water, the DOPC standard solution, and 4-deuterated methanol ($k=1-4$) at the CH_3 , CH_2 , and H_2O Raman bands ($i=1-3$). The intensities are calculated after the background subtraction and flat field correction from the average of the whole image at the single z plane as described above (Supplementary Fig.5c). The matrix C is defined as a 4×4 matrix where C_{jk} denotes the concentration of protein, lipid, water and deuterated methanol fractions ($j=1-4$) in the standard samples ($k=1-4$). The concentration is expressed in the unit of volume fractions between 0 and 1. The decomposition matrix is computed by solving for M that satisfies $C = MS$. This can be computed in a single line using right matrix division in Matlab $M = C/S$, which gives a 4×3 matrix that maps three Raman bands to protein, lipid, water and deuterated methanol fractions. The last row that maps to deuterated methanol is not necessary and was dropped out (they are also inaccurate as the SRS signal is practically zero in all three Raman bands), resulting in a final 3×3 matrix form of M .



Supplementary Figure 6. Flow chart of calibration steps. (a) Four calibration samples are assembled on a slide glass. (b) Concentration matrix of a representative calibration samples in units of volume fraction. (c) Representative raw SRS intensity images of 4 calibration standard samples at the CH_3 , CH_2 , and H_2O Raman bands. (d) Flat field correction masks are computed for each Raman band. (e) The SRS signal matrix is calculated by taking the average of the whole image after background subtraction and flat-field correction. (f) Decomposition matrix is computed by solving for M in $C=M*S$ where S is the SRS signal matrix and C is the concentration matrix.

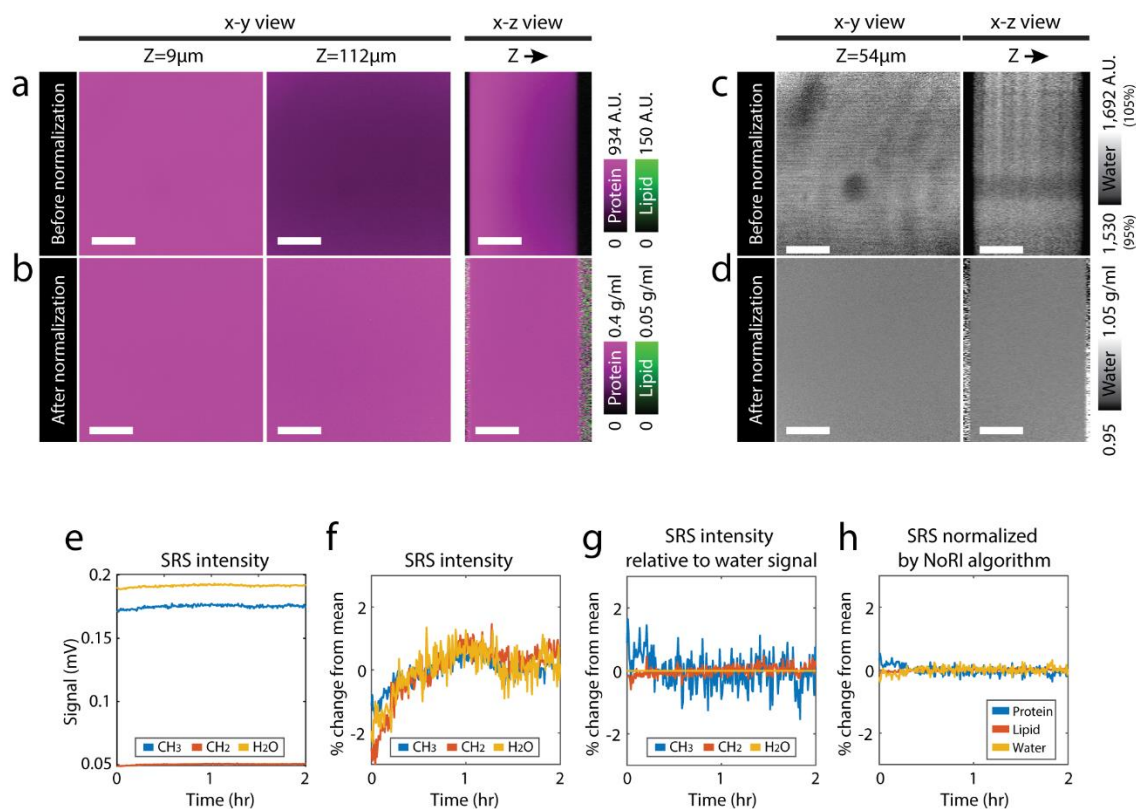
1.7. Applying the decomposition matrix to sample data

The decomposition matrix is applied to the sample images after background subtraction and flat-field correction. Spectral decomposition is applied to individual pixels independently by multiplying the 3x3 decomposition matrix to the 3-component vector of the SRS intensities at the CH₃, CH₂, and H₂O Raman bands of each pixel. This matrix multiplication can be simplified by linearizing the image data as a 1xN vector. The linearized images of three Raman band can be stacked as a single 3xN matrix, S. The spectral decomposition becomes matrix multiplication of a 3x3 matrix M with a 3xN matrix S. This result is a 3xN matrix where each row represents the pre-normalization concentration of the respective chemical species. Each row can be reshaped to the original image size to obtain the decomposition image.

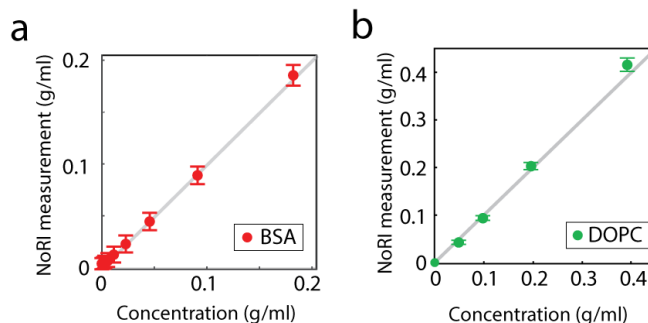


Supplementary Figure 7. Flow chart of sample data processing steps. (a) Sample is imaged at the CH₃, CH₂ and H₂O Raman bands and the background level is subtracted. (b) Flat field masks are generated from the calibration data. (c) Sample images are divided by the flat field correction mask of the matching Raman band. (d) A decomposition matrix is acquired in the calibration step. (e) The decomposition matrix is applied to each pixel, generating pre-normalization concentration images. (f) The pre-normalization protein, lipid, and water images are summed at each pixel to compute the attenuation map. (g) Each pre-normalization image is divided by the sum image (attenuation map) to compute the absolute concentration image in the unit of volume fractions. (h) Volume fraction is multiplied by the density of pure BSA, DOPC, and water to convert to mass concentration.

1.8. Demonstration of NoRI measurements



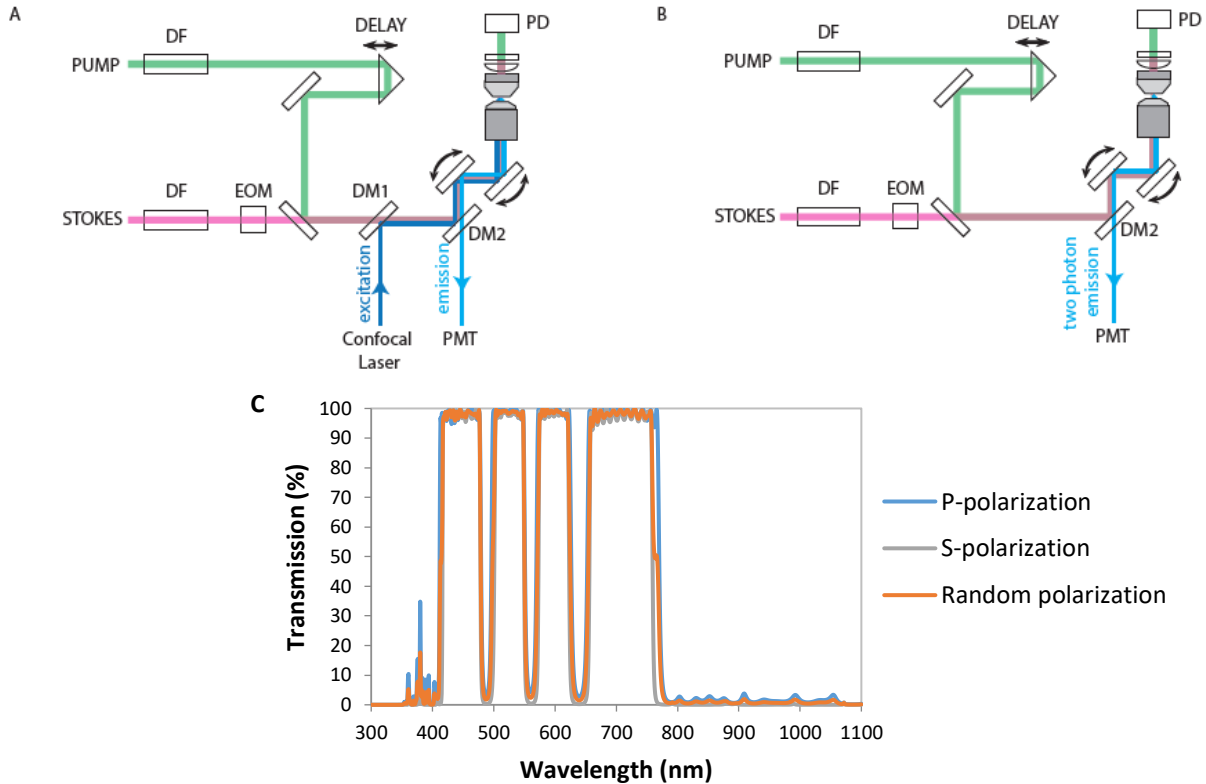
Supplementary Figure 8. NoRI eliminates spatial and temporal variability in measurements. (a) Pre-normalization images of protein and lipid concentration of 33%(w/w) BSA solution. The solution is sandwiched between a coverslip and a slide glass. Signal intensity diminishes with z depth due to optical aberration caused by the high refractive index of the solution. Scale bar, 50 μm . (b) NoRI normalization of (a) removes the effect of optical aberration and enables accurate measurement of concentration throughout sample volume. Scale bar, 50 μm . (c) Pre-normalization water concentration images of water sample shows stationary spatial variation caused by imperfections of the optical system and detector. Scale bar, 50 μm . (d) NoRI normalization is applied to (c) and removes the stationary spatial variation. Scale bar, 50 μm . (e) SRS intensity from a BSA solution is acquired at the CH₃, CH₂ and H₂O bands every 30 seconds for 2 hours. (f) Data in (e) is plotted as percentage changes relative to the mean. Temporal fluctuation due to environmental and instrumental instability is about 2% and shows a similar trend in all 3 Raman bands. (g) SRS signal fluctuation relative to the H₂O band signal. The CH₃ band and CH₂ bands are divided by H₂O band signal at each time point. (h) NoRI normalization eliminates temporal fluctuations better than relative measurement to the H₂O band signal.



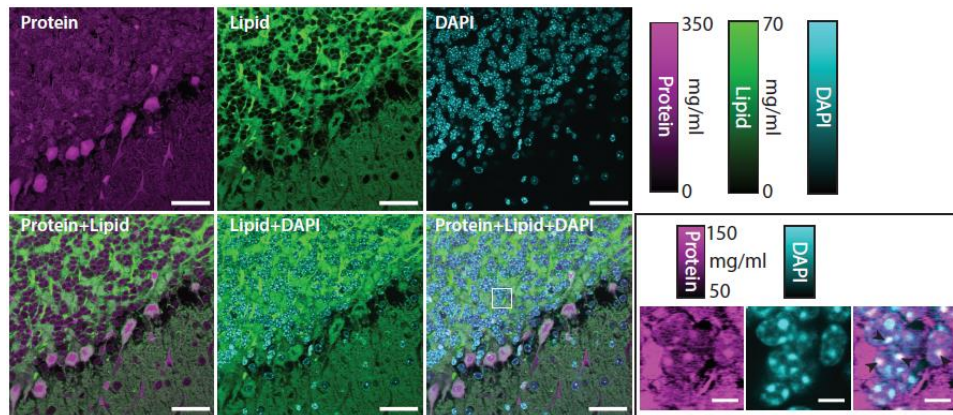
Supplementary Figure 9. NoRI measurement of (a) protein concentration of BSA solutions and (b) lipid concentration of DOPC solutions show good agreement with the actual concentration. In DOPC titration, organic solvent (deuterated methanol) was used in place of water for normalization. Error bars indicate standard deviations.

1.9. Simultaneous fluorescence imaging with NoRI

NoRI is compatible with fluorescence imaging and simultaneous or tandem acquisition of confocal and two photon fluorescence is possible using a custom 5-band filter (Supplementary Fig. 10A-B DM2; Chroma, zt405/488/561/640/NIR-xr-rpc-UF2). An example of tandem fluorescence and NoRI imaging is shown in Supplementary Fig. 11.



Supplementary Figure 10. Schematics of simultaneous or tandem acquisition of fluorescence with NoRI. (A) Light path for simultaneous confocal fluorescence and SRS imaging. DM1 is a longpass filter for combining combine confocal excitation lasers (405, 488, 561, 640 nm) with near-infrared lasers for NoRI (770 – 1045 nm). DM2 is a customized 5-band pass filter. (B) Light path for simultaneous two photon fluorescence and SRS imaging. Confocal pinhole is fully opened. (C) Transmission spectra of the custom 5-band filter.



Supplementary Figure 11. Tandem acquisition of DAPI fluorescence and NoRI. DAPI fluorescence by confocal fluorescence and protein and lipid NoRI images of fixed mouse cerebellum. Scale bar, 40 μm. (Inset) Magnified view of DAPI and protein puncta. Overlapping DAPI and protein puncta are marked with arrowheads. Inset scale bar, 5 μm.

2. Cell culture sample preparation

A7 human melanoma cell line was purchased from ATCC (catalog no. CRL-2500). Wild-type Madin-Darby canine kidney (MDCK) cell line is a kind gift from Dr. Chan Young Park lab, Harvard school of public health. This cell line has been reported in several publication from the group mentioned above. Cells were cultured in low glucose DMEM (Gibco catalog no 11054-001) in presence of 10% FBS (Gibco catalog no. 10437-028) in standard T75 flasks (BD) in a humidified incubator kept at 37°C. For imaging experiments, cells were dislodged from the T75 flask using 0.25% trypsin (Gibco catalog no. 15090-046) with 100 µM EDTA solution, and replated in 60 mm glass bottom petri plates (Cellvis catalog no. D60-30-1.5-N). For the mitotic cell measurement, cells were allowed to grow 2 days after plating before imaging. Hoechst 33342 (Thermo scientific catalog no. R37605) and CellMask deep red plasma membrane stain (ThermoFisher, cat no. C10046) were added 30 min before imaging. Senescent cells were prepared by plating cells on glass bottom petri-plates as described above. Cells were allowed to adhere to the glass surface overnight and Doxorubicin (100 ng/mL) is added the next morning to induce senescence. Cells were kept under Doxorubicin treatment for 48 Hrs.

Polyacrylamide gel on glass glass-bottom 60 mm plates (cellvis) was prepared as followed: Polyacrylamide gel substrate of defined stiffness was adapted from the protocol mentioned by Trepate et Al⁹. Briefly :1 ml of Bind-Silane binder was added to the glass surface of the plate, and incubated at room temperature for 1 hour. Bind-Silane stock was prepared as followed: 400ml distilled water+320 µl glacial acetic acid (Fisher Scientific) +320µl 3-(Trimethoxysilyl)propyl Methacrylate (stabilized with BHT) (TCI M0725). After 1 hour of incubation the binder solution is removed from the glass surface and the binder coated surface was washed with 2 ml distilled water (5 times). To obtain precise height acrylamide gel, a donut shaped ring (inner diameter 18mm), cut from bio-compatible double-sided tape of 120micron thickness (Grace Bio-Labs SA-S-1L) was placed at the center of glass plate and 45 µl of acrylamide gel solution (Supplementary Table 2) was dispensed onto the center of the glass-bottom plate. A 25 mm round coverslip was placed over the gel droplet to flatten the gel and the plate was kept at room temperature for 30 minutes for the gel polymerization to occur. After 30 min, 5 ml distilled water was added to the plate to submerge the gel and the overlaying coverslip was removed (for efficient coverslip removal, glue on the double-sided tape needed to be weakened. We place a circular acrylic disc on the double-sided tape before putting the gel droplet and remove it to wear out the glue). After coverslip removal, water was aspirated out from the plate.

Supplementary Table 2. Recipe for polyacrylamide gels.

E (Pa)	600	19200
G (Pa)	200	6400
40% Acrylamide (BioRad 16120140)	75µl	188µl
2% Bisacrylamide (BioRad 1610142)	29µl	118µl
Water	795µl	593µl
TEMED (Invitrogen HC2006)	1µl	1µl
APS (10mg/ml) (Thermo 17874)	100µl	100µl

Sulfo-SANPAH and collagen coating of gel: Sulfo-SANPAH crosslinker (ProteoChem c1111-100mg) was dissolved in DMSO (50mg/ml stock solution). 40 µl of sulfo-SANPAH stock solution was dissolved in 10 ml PBS (supplemented with 50mM HEPES, final concentration (Sigma)). 500µl SANPAN in HEPES-PBS, was pipetted on the gel surface and the plate was kept under UV lamp (Analytikjena UVP xx-15L, 15-Watt, 365 nm) for 10 minutes for SANPAH activation. After 10 minutes, SANPAH solution was removed and the gel was washed three times with HEPES-PBS (2 ml) followed by another 3 washes in PBS (2 ml). Type I Collagen Solution, (3 mg/ml Bovine, Advanced Biomatrix #5005), was diluted in PBS to obtain a final concentration of 10µg/ml and 2 ml collagen solution was added to the plate. The plate was kept in 4°C overnight. Next morning

the collagen solution was removed and the gel surface was washed with PBS. After washing, cells were seeded on collagen coated gel surface.

3. Animal protocols

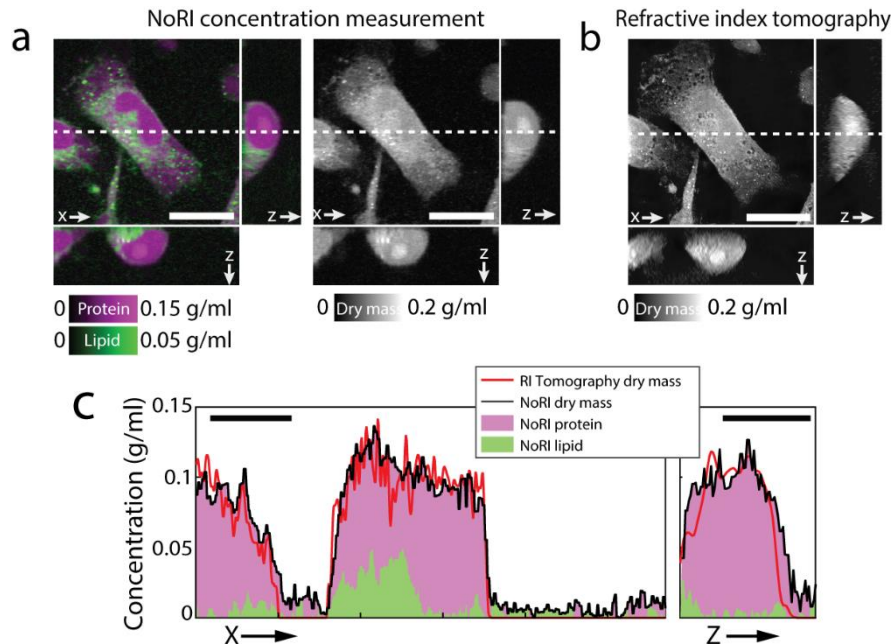
Wild type mouse tissues were collected from 8-12 week old male mice in accordance with the procedure approved by Institutional Animal Care and Use Committee (IACUC) at Harvard University. Transgenic female APP-PS1 mice and age-matched wild type (WT) C57 black 6 female mice were purchased from Jackson Laboratory. GDF15-KO mouse tissue was a kind gift from Jui-Hsia Weng. This mouse strain is, without toxin challenge, indistinguishable from WT for our purpose. For live imaging of zebrafish embryos, AB strain wild type fish was used. All fish were kept at 28°C on a 14-hour-light/10-hour-dark cycle. Embryos were collected from natural crosses. The chorion was removed manually prior to imaging. All fish-related procedures were carried out with the approval of Institutional Animal Care and Use Committee (IACUC) at Harvard University. All animal experiments were approved by the Institutional Animal Use and Care Committee at Harvard Medical School and Massachusetts General Hospital.

4. Tissue sample preparation

All mouse tissues were dissected from euthanized animals and immersion fixed in 4% formaldehyde at 4°C for 24 hours. Mouse cerebellum was perfusion fixed with 4% formaldehyde at 4°C for 24 hours. The fixed tissues, except for cartilage and APP-PS1 and WT brains, were embedded in 2% agarose and sectioned to 40–100 μm thickness using a vibrating microtome (Precisionary Instruments, VF-300-0Z). Fixed cartilage tissues were embedded in BSA-gelatin gel cured with formaldehyde in room temperature overnight, and sectioned by a vibrating microtome (Leica, VT1000M). Fixed brains were transferred into 30% sucrose at 4°C until the tissue sunk in. Then the tissue was frozen in OCT to be sectioned into 25- μm slices in a cryostat. The brain sections were washed of sucrose with phosphate buffered saline. The tissue sections were transferred to phosphate buffered saline bath and stored at 4°C until imaging. For imaging, a tissue section was sealed between a coverglass and a slide glass with phosphate buffered saline using a double-sided tape spacer (Grace Biolabs, SS1X13) or using nail polish as sealant.

5. Tomographic phase microscopy imaging protocol

For tomographic phase imaging, HeLa cells were cultured in a glass bottom dish (Cellvis, D60-30-1.5-N) using a culture insert (Ibidi, 80209) to restrict growth area. The cells were fixed with 4% formaldehyde in the room temperature for 20 minutes and washed with phosphate buffered saline 3 times. A top coverslip is placed over the fixed HeLa cells with an imaging spacer of 120 μm thickness (Grace Biolabs, SS1X20). Tomographic phase images were acquired using a commercial tomographic phase microscope (Tomocube, HT-2) using a 60x water immersion objective lens and a water immersion condenser lens. The dry mass concentration was calculated from the refractive index tomogram assuming average refractive index increment of $dn/dc = 0.19 \text{ ml/g}^{10}$.

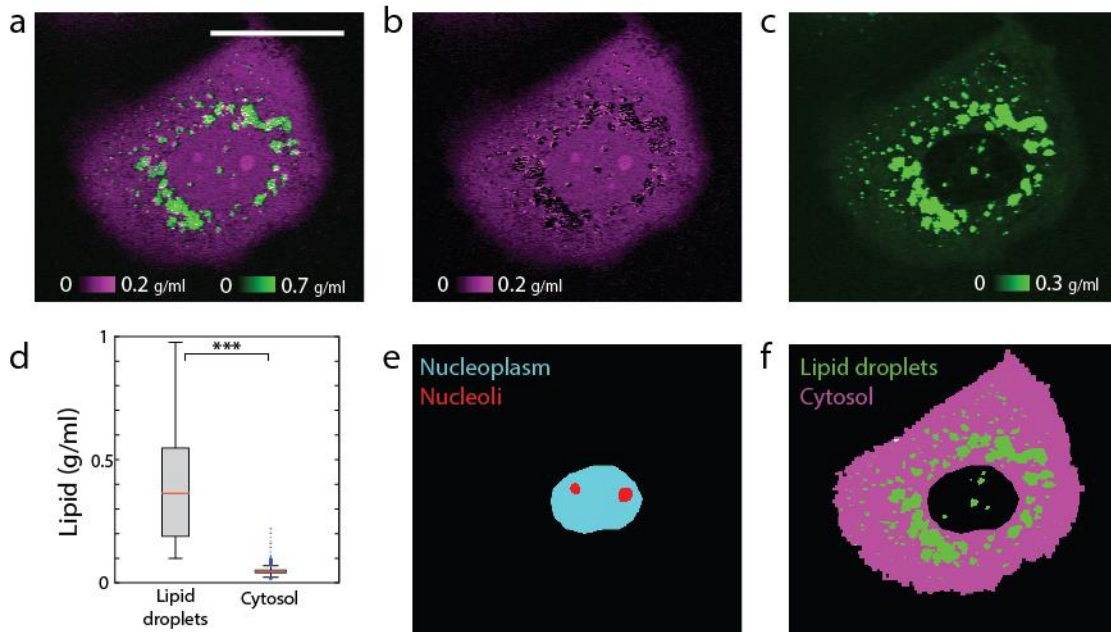


Supplementary Figure 12. Comparison of NoRI measurement and Tomographic Phase microscopy (a) Protein and lipid NoRI image of a fixed HeLa cell. Dry mass is the sum of protein and lipid masses. Scale bar, 20 μm . Whole cell mass integrated over the volume was 430.2 pg. (b) Dry mass concentration of the same cell measured by refractive index tomography microscope (Tomocube, HT-2). Average refractive index increment of 0.19 ml/g is assumed to compute dry mass concentration from refractive index contrast¹. Scale bar, 20 μm . Whole cell mass integrated over the volume was 434.2 pg. (c) Mass concentration profile along the x- and z-cross sections marked by dashed lines in (a) and (b). Dry mass density measured by NoRI is in good agreement with dry mass measured by refractive index tomography. Pearson correlation coefficient of NoRI dry mass density and refractive index tomography dry mass density is $r=0.736$. Scale bar, 10 μm .

6. Image segmentation methods

6.1. Image segmentation based on protein and lipid concentrations

Differences in protein and lipid concentrations were used for segmentation of cell body, nucleus, and lipid droplets in Fig. 2c. To segment the cell body, a threshold of 0.0217 g/ml was applied to the protein concentration image, followed by ‘Fill Holes’ and ‘Despeckle’ functions of ImageJ. To segment the nucleus, a 2-fold scaled lipid image was subtracted from the protein image, from which nuclear area was segmented by a thresholding operation. The segmentation was cleaned up by removing areas under 100 μm^2 in size. Lipid droplets were segmented by a threshold operation based on lipid concentration. The lipid droplet threshold was adjusted between 0.1-0.2 g/ml depending on the cytosolic lipid concentration (Supplementary Fig. 12). Whether the protein and lipid concentrations provide sufficient contrast at the cell body boundary depended on the cell and tissue types. When simple thresholding operations were not sufficient, we found that ImageJ plug-in trainable WEKA segmentation provides a more flexible solution for image segmentation of cultured cells¹¹. Single cell segmentation in complex tissue environments can be more challenging and may require optimization of machine learning algorithm or the use of fluorescence labels of the cell membrane.



Supplementary Figure 13. X-Y cross section image and organelle segmentations of a senescent MDCK cell. (a) Protein concentration (magenta) and lipid concentration (green). Lipid droplets are clearly visible. Scale bar, 50 μm . (b) Protein concentration. (c) Lipid concentration. Color display range for lipid is zoomed in to highlight the low concentration lipid in the cytosol compartment. (d) Distribution of lipid concentrations of lipid droplets (0.387 ± 0.208 g/ml) and cytosol (0.047 ± 0.013 g/ml) in the cell. The large difference facilitates lipid droplet detection ($p < 0.001$). (e) Segmentation of nucleolus by trainable WEKA segmentation of nucleus protein image. (f) Lipid droplet and cytosol segmentation by thresholding the lipid image.

6.2. Image segmentation of brain tissue NoRI images

Protein aggregates (amyloid plaques) and lipid aggregates are detected from NoRI images of APP-PS1 brain tissue based on protein and lipid concentration using Trainable WEKA Segmentation tool¹¹ and OrientationJ¹² in imageJ. Using the WEKA tool, a protein concentration image is first classified using two features, protein dense plaques and “the rest” which includes rest of the tissue and background areas. The lipid concentration image is classified using three features, white matter which has the highest concentration of lipid, neuropil, constituting the gray matter, and lipid aggregates, which show a higher lipid concentration than the neuropil but a lower lipid concentration than white matter. Segmentation of protein plaques is completed by applying a size threshold of 200 μm^2 to the WEKA segmentation output of the protein dense plaque class. Lipid aggregates segmentation is calculated from the WEKA segmentation output of lipid aggregate class after removing crosstalk from the myelin class. The crosstalk appears at the border between the two classes owing to the imperfect WEKA classifier training and can be improved by subtracting myelin adjacent area computed from OrientationJ operation. OrientationJ detects spatial coherence of features and is particularly suitable to detect the cable-like morphology of myelin sheaths. The myelin-adjacent area is computed by applying the threshold operation to the spatial coherence output of OrientationJ; this mask is then subtracted from lipid aggregate class segmentation. To obtain the final segmentation for lipid aggregates, a size threshold of 35 μm^2 is applied. Myelinated axons are segmented by their lipid concentration, 0.148 g/ml or higher. The cell body is segmented by using a lipid concentration threshold at 0.041 g/ml. Neuropil segmentation is computed from the WEKA neuropil class output by subtracting the areas of cell body, amyloid plaques and myelin.

7. Statistics

All statistical analyses were performed in Matlab (R2020a). Box plots represent the median, 25th and 75th percentiles and whiskers with staples represent the minimum and maximum of non-outlier samples. Outliers are plotted as black filled circles. Violin plots are plotted using VIOLIN.m in Matlab¹³. Bars inside violin plots represent the median. Correlations between two distributions and corresponding p-values were computed using CORRCOEFF.m function in Matlab. Comparisons between two distributions were performed with two-sample *t*-test using TTEST2.m function in Matlab.

8. Supplementary theory of NoRI

The linear dependency of SRS intensity to the analyte concentration can be described by an equation $\mathbf{M}_{ij}^{(k)} \mathbf{S}_{ik} = \mathbf{C}_{jk}$ (Eq. 1), where \mathbf{S}_{ik} is the SRS signal at the *i*-th Raman band (*i*=CH₃, CH₂ and H₂O) of the *k*-th reference sample (*k*=BSA, DOPC and water samples) and \mathbf{C}_{jk} is the volume concentration of the *j*-th component (*j*=protein, lipid and water) of the *k*-th sample in the unit of volume fraction (ml/ml)¹⁴. $\mathbf{M}_{ij}^{(k)}$ is the decomposition matrix for the *k*-th sample. In Supplementary Methods 1.5 we described the optimal protocol for measuring the SRS intensity of the calibration reference samples. This minimizes sources of intensity variation other than the sample's chemical composition and the intrinsic Raman cross sections of the chemical components and assures quantitative consistency of the decomposition matrix \mathbf{M}_{ij} across different samples (*k*=BSA, DOPC and water samples). This allows us to concatenate the equations $\mathbf{M}_{ij} \mathbf{S}_{ik} = \mathbf{C}_{jk}$ for all *k* samples. The decomposition matrix is next solved by a simple matrix inversion $\mathbf{M}_{ij} = \sum_k \mathbf{C}_{jk} \mathbf{S}_{ik}^{-1}$ (Eq. 2). The inverse of the decomposition matrix \mathbf{M}_{ij}^{-1} is interpreted as the SRS intensity of the *i*-th Raman band measured from a pure material of the *j*-th component. It is proportional to the Raman cross section of the molecule σ_{ij} as well as to the efficiency of the imaging system \mathbf{A}_{i0} as optimized for the imaging of calibration standards; that is, $\mathbf{M}_{ij}^{-1} = \sigma_{ij} \mathbf{A}_{i0}$, or $\mathbf{S}_i = \sum_j \sigma_{ij} \mathbf{A}_{i0} \mathbf{C}_j$ (Eq. 3). While the Raman cross section σ_{ij} is an intrinsic property of the chemical constituent, the efficiency of the microscope \mathbf{A}_{i0} is affected by the optical aberration of the imaging system and the detector efficiency. Spectral decomposition is applied by matrix multiplication of the decomposition matrix with SRS images at the CH₃, CH₂ and H₂O Raman bands: $\sum_i \mathbf{M}_{ij} \mathbf{S}_i(\vec{r})$ (Eq. 4).

When imaging samples, the light scattering and aberration caused by the sample introduces an extra attenuation factor $\mathbf{A}_X(\vec{r})$ to the signal, which can be expressed as $\mathbf{S}_i(\vec{x}) = \sum_j \sigma_{ij} \mathbf{A}_{i0} \mathbf{A}_X(\vec{r}) \mathbf{C}_j(\vec{r})$ (Eq. 5). As we argue below, we assume that the sample induced attenuation factor is independent of the Raman bands. When spectral decomposition is applied to sample images, by multiplying the decomposition matrix with the SRS intensity, we do not get the true concentration because of this factor. Instead, the output of spectral decomposition is proportional to the concentration of respective chemical components and also to the spatially heterogeneous attenuation: $\sum_i \mathbf{M}_{ij} \mathbf{S}_i(\vec{r}) = \mathbf{A}_X(\vec{r}) \mathbf{C}_j(\vec{r})$ (Eq. 6). The unknown attenuation factor varies with position and with each sample and limits the quantitative interpretation of spectral decomposition. The sample attenuation $\mathbf{A}_X(\vec{r})$ can be estimated by making a reasonable approximation that the major chemical components (protein, lipid and water) occupy 100% of the sample volume. This is expressed by $\sum_j \mathbf{C}_j = 1$ (Eq. 7) where *j*=protein, lipid and water. Using Eq. 7, the sum of Eq. 6 over *j*=protein, lipid and water is equal to $\mathbf{A}_X(\vec{r}) = \sum_{ij} \mathbf{M}_{ij} \mathbf{S}_i(\vec{r})$ (Eq. 8). $\mathbf{A}_X(\vec{r})$ measures the collective sample property that attenuates the SRS intensity at each voxel which includes the presence of scatterers above and below the imaging plane (Supplementary Fig.7f). It is defined throughout the sample imaging volume and serves as the light scattering normalization mask. Absolute concentration of *j*-th component in volume fraction $\mathbf{C}_j(\vec{r})$ is obtained by dividing the spectral decomposition in Eq. 6 by the normalization mask $\mathbf{A}_X(\vec{r})$ from Eq. 8. Due to the general nature of the linear relationship in Eq. 5, light scattering normalization may be applied to other nearby Raman bands provided that the light

scattering property of the laser does not change significantly between the applied band and the CH₃, CH₂ and H₂O bands. Additional information on the wavelength dependence of tissue light scattering in the near-infrared range is included in the following section.

9. Wavelength dependence of light scattering: impact on imaging depth limit

The NoRI algorithm corrects for the effect of light scattering on the basis that the light scattering is same for all pump beam wavelengths. In fact, the intensity attenuation from tissue light scattering and absorption is nearly independent of wavelength in the relevant wavelength range¹⁵. The pump beam wavelength changes between 770 nm and 805 nm to select different Raman bands. The intensity I at depth z in a tissue with reduced scattering coefficient $\mu'_s(\lambda)$ is described by $I(z, \lambda) = I_0 e^{-\mu'_s(\lambda)z}$. The reduced scattering coefficient of common tissues in the range, 770–805 nm, is on the order of 1-2 mm⁻¹, and the wavelength dependent change of this value is less than 0.2 mm⁻¹ between 770–805 nm¹⁶. The wavelength dependent difference in light scattering can be described using $I(z, \lambda_1)/I(z, \lambda_2) = I_0 e^{-(\mu'_s(\lambda_1) - \mu'_s(\lambda_2))z}$. The depth z where the difference reaches 1/e is $z = 1/(\mu'_s(\lambda_1) - \mu'_s(\lambda_2))$. Similarly, the depth z where the attenuation deviates by 1% is $z = \log(1.01)/(\mu'_s(\lambda_1) - \mu'_s(\lambda_2))$. We simulated the imaging depth at which the wavelength dependent differences in reduced scattering length affect 1% and 2% of intensity using the average number reported in Ref¹⁶ (Supplementary Table 3). Various tissues show less than 2% difference between 770 and 805 nm within the imaging depth limit of SRS microscopy (90-120 μm)¹⁷.

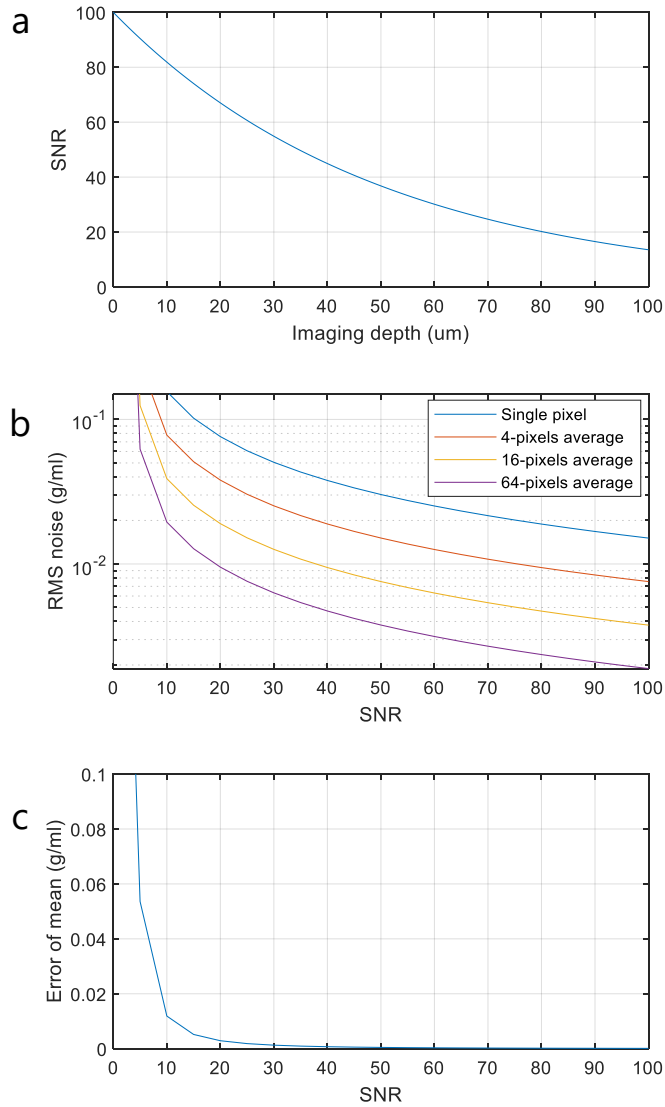
Supplementary Table 3. Wavelength dependence of light scattering of various tissues

Tissues	$\mu'_s(\lambda)$ (mm ⁻¹)				$\mu'_s(770\text{nm}) - \mu'_s(805\text{nm})$ (mm ⁻¹)	1/e difference depth (mm)	1% difference depth (mm)	2% difference depth (mm)
	$\lambda=500$ nm	$\lambda=770$ nm	$\lambda=800$ nm	$\lambda=805$ nm				
Skin	4.6	2.49	2.36	2.34	0.15	6.6	0.028	0.056
Brain	2.42	1.21	1.13	1.12	0.08	12.0	0.052	0.103
Breast	1.68	1.07	1.02	1.02	0.05	20.5	0.089	0.176
Bone	2.29	1.68	1.64	1.63	0.05	19.0	0.082	0.163
Other soft tissues	1.89	1.08	1.03	1.02	0.06	16.6	0.072	0.143
Other fibrous tissues	2.71	1.34	1.26	1.25	0.09	10.7	0.046	0.092
Fatty tissue	1.84	1.38	1.34	1.34	0.04	24.7	0.107	0.212

10. Depth dependence of the measurement sensitivity of the concentration

We simulated the effect of signal to noise ratio (SNR) on the sensitivity. In particular, SNR decreases as a function of imaging depth as is depicted in Supplementary Fig. 13a. The detector noise was 26 nA as measured by the standard deviation of photo detector readout when the detector is illuminated with pump beam and the Stokes beam is absent from the sample. The SRS signal of tissue samples is around 2 μA (SNR=100) near the surface and exponentially decreases with imaging depth. 1/e² attenuation depth of various murine tissues are in the range of 90 - 120 μm ¹⁷. We used 100 μm for our simulation. The noise was generated from a normal distribution with 0 nA mean and standard deviation of 26 nA. As the noise in the CH₂, CH₃ and H₂O Raman bands are independent, we denote the three instances of noise by a 3x1 vector \vec{n} . Spectral decomposition transforms the detector signal $\vec{s} + \vec{n}$ to $M(\vec{s} + \vec{n})$, where \vec{s} is true signal in the CH₂, CH₃ and H₂O Raman bands and M denotes an experimentally measured decomposition matrix. $M\vec{s}$ is a 3x1 vector whose components are proportional to the true concentration in protein, lipid and water fractions (\vec{c}). There is an arbitrary unit constant ρ that satisfies $M\vec{s} = \rho\vec{c}$ for all \vec{s} . $M\vec{n}$ is a 3x1 vector whose components represent the noise in protein, lipid and water fractions. They had mean value of 0 and standard deviations of 20, 26, and 28 (A.U.) for protein, lipid, and water fractions, respectively. The normalization step transforms $M\vec{s} + M\vec{n}$ to

absolute concentration in volume fraction $\vec{C} = \frac{M\vec{s}+M\vec{n}}{\sum(M\vec{s}+M\vec{n})}$, where the sum in the denominator is over protein, lipid and water fractions. Note that when SNR equals 1, the mean of $M\mathbf{s}_i$ equals the RMS size of $\langle M\mathbf{n}_i \rangle$, for each i =protein, lipid or water. Therefore, we can obtain $\rho c_i = \langle M\mathbf{n}_i \rangle$. Since c_i , the concentration in volume fraction, is in the range of 0 - 1, we can simulate different SNR by parameterizing ρ . We computed the mean and RMS noise of the absolute concentration \vec{C} for concentration range of 0 - 1 (v/v) and SNR range of 1 to 100 at steps of 5 (Supplementary Fig. 13b-c). The volume fraction is converted to w/v concentration using the density of water (1 g/ml). The sensitivity at 100 SNR was 0.015 g/ml (1.5% w/v) in agreement with the experimental measurement. At the 1/e attenuation depth (50 μm in this simulation), the noise reaches 0.040 g/ml (4% w/v) for single pixels and 0.020 g/ml (2% w/v) for average of 4 pixels. By averaging 64 pixels (equivalent to 3.3 μm x 3.3 μm area), noise can be kept under 0.015 g/ml (1.5% w/v) at the 1/e² attenuation depth (100 μm).



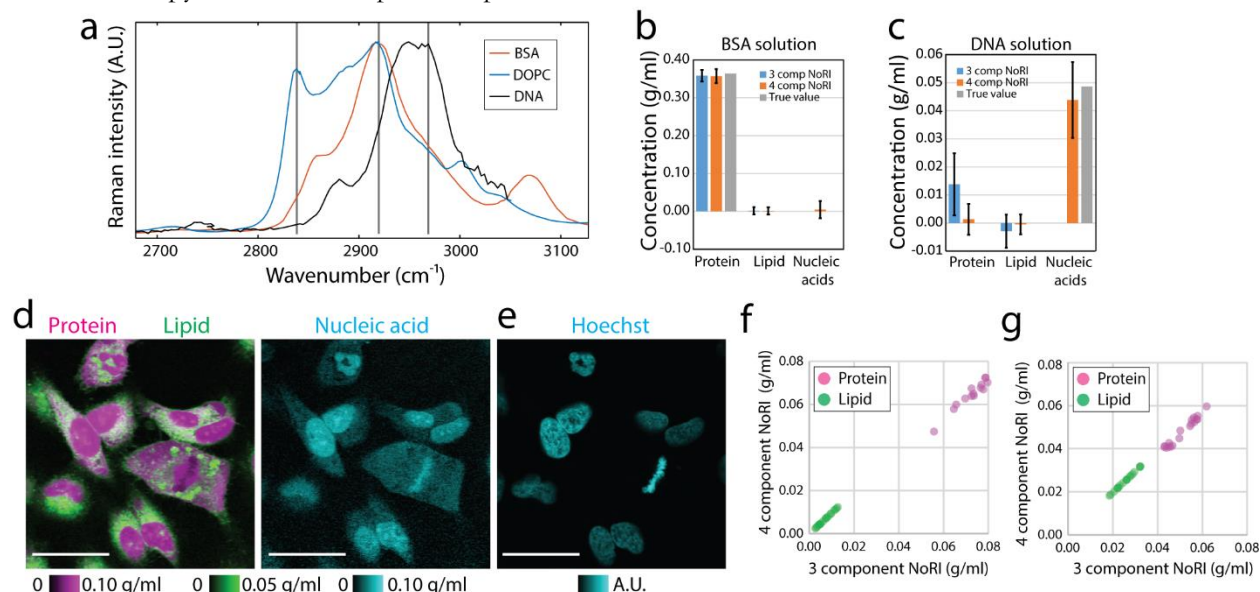
Supplementary Figure 14. Sensitivity of concentration as a function of signal-to-noise ratio (SNR). (a) SNR decreases with imaging depth. (b) RMS noise as a function of SNR. (c) Error of mean value as a function of SNR.

11. Limitations of the absolute concentration measurement by NoRI

To assure the accuracy of the absolute concentration measurement by NoRI, it should be applied to samples where the following conditions are satisfied: (11.1) protein, lipid and water constitute most of the chemical composition, (11.2) calibration standards (BSA and DOPC) are good approximations of the average proteome and lipidome of the sample in terms of their Raman spectra, and (11.3) pigments are absent or bleached as they can cause non-Raman background through two-color two-photon absorption of the pump and Stokes beams^{18,19}.

11.1. Chemical components of sample

NoRI, based on the CH₃, CH₂ and H₂O channels, provides high accuracy for cells and tissues where protein, lipid and water makes up nearly 100% of the chemical composition. For mammalian cells whose combined fraction of protein, lipid and water is greater than 93% of the wet mass²⁰, the percentage error arising from neglected 7% other component is small in absolute size for components other than water because it is multiplicative (7% error of 0.1 g/ml is ± 0.007 g/ml). For tissues with very low lipid content, NoRI normalization scheme can be adapted to use only the CH₃ and H₂O channels. Such approach was used to analyze water content in eye lens tissue by confocal Raman microscopy²¹. Normalization by the standard NoRI scheme can be generalized to more than 4 chemical components to improve accuracy when the sample has significant amount of other substances (Supplementary Fig. 15). For example, yeast and bacterial cells have a high nucleic acids content²⁰, and 4-channel NoRI including nucleic acids would be more appropriate. Increasing the number of Raman bands will, nevertheless, increase acquisition time but will benefit from hyperspectral SRS microscopy and advanced spectral separation schemes^{22,23}.



Supplementary Figure 15. 4-component NoRI for quantitative measurement of protein, lipid, nucleic acids, and water. (a) Raman spectrum of BSA, DOPC and salmon sperm DNA. The contribution from solvents is subtracted and the effect of pulse overlap is normalized according to Supplementary Fig. 3. Vertical lines indicate the positions of the CH₂, CH₃, and nucleic acids bands from the left to the right. These three Raman bands are measured along with the H₂O band to spectrally separate proteins, lipids, nucleic acids and water. The laser settings for selecting these bands are summarized in Supplementary Table 1. (b-c) A comparison of concentration measurements of pure samples by 3-component NoRI vs 4-component NoRI. DNA shows partial cross talk with protein measurement. (d) NoRI imaging of protein, lipid, and nucleic acids in live HeLa cells measured by 4-component NoRI. Raw SRS images are acquired using frame averaging of 16 to suppress detector noise. Scale bar, 40 μm. (e) Sample is co-stained with Hoechst 33342 and imaged using confocal scanning microscopy. Nucleic acid rich area in the NoRI image co-localizes with nuclei in the Hoechst fluorescence image. (f-g) Comparison of protein and lipid measurement in HeLa cells by 3-component NoRI vs 4-component NoRI in nucleus (f) and in cytoplasm outside nucleus (g) (N=18).

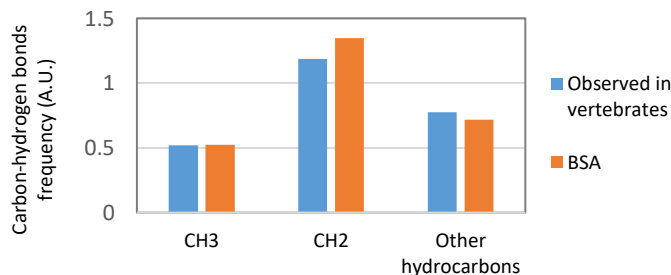
11.2. Calibration reference materials

We chose BSA and DOPC as the calibration reference materials because BSA has a similar Raman spectrum in the CH₂ and CH₃ bands compared to the average vertebrate proteome²⁴ and DOPC is one of the most abundant lipids in cell membranes. They are both economical and available as a highly purified material in large quantity, and as discussed below, are generally good starting material when considering the choice of calibration standards.

Whether BSA is a good representation of sample proteome is solely determined by their high wavenumber Raman spectrum. This can be estimated from the hydrocarbon frequency of the sample proteome which can be counted from the amino acid frequency. As shown in Supplementary Fig. 16, the frequency of methyl groups, methylene groups and other hydrocarbons of BSA is similar to that of the average vertebrate proteome²⁵. When a few types of proteins dominate the tissue proteome, it should be checked whether BSA is a good representation of sample proteome's Raman spectrum. In such cases, the dominant protein or tissue protein extract can be used as the calibration material²⁴.

Supplementary Table 4. Frequency of methyl and methylene groups in the average vertebrate proteome²⁵ and in bovine serum albumin. BSA amino acid frequency from <https://www.uniprot.org/uniprot/P02769>

Amino acids	Amino acids	CH ₃ in side group	CH ₂ in side group	Other C-H bonds	Observed Frequency in Vertebrates	Frequency in BSA
Alanine	A	1			7.4%	8.1%
Arginine	R		3		4.2%	3.9%
Asparagine	N		1		4.4%	2.4%
Aspartic Acid	D		1		5.9%	6.9%
Cysteine	C		1		3.3%	6.0%
Glutamic Acid	E		2		5.8%	10.1%
Glutamine	Q		2		3.7%	3.4%
Glycine	G			1	7.4%	2.7%
Histidine	H		1	2	2.9%	2.9%
Isoleucine	I	2	1	1	3.8%	2.4%
Leucine	L	2	1	1	7.6%	10.5%
Lysine	K		4		7.2%	10.1%
Methionine	M	1	2		1.8%	0.7%
Phenylalanine	F		1	5	4.0%	4.6%
Proline	P		2		5.0%	4.8%
Serine	S		1		8.1%	4.8%
Threonine	T	1		1	6.2%	5.7%
Tryptophan	W		1	5	1.3%	0.3%
Tyrosine	Y		1	4	3.3%	3.4%
Valine	V	2		1	6.8%	6.2%

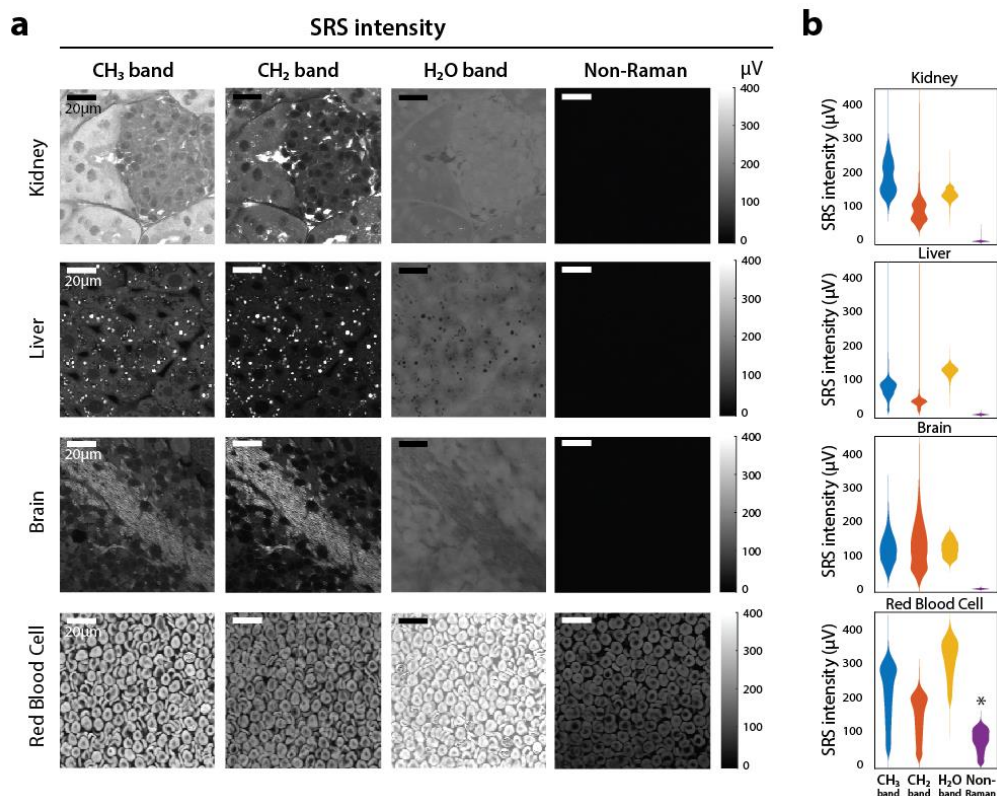


Supplementary Figure 16. Carbon-hydrogen bonds frequency in vertebrate proteome and bovine serum albumin. Bonds frequency are calculated from Supplementary Table 3.

Although DOPC is the most abundant lipid in cell membranes, lipid droplets are composed of triacylglycerol and cholesterol esters, and spectral decomposition using DOPC reference spectra does not calculate the accurate lipid concentrations in these lipid droplets. As discussed above, we adopted a two-step approach in which lipid droplets are segmented by thresholding operation on lipid concentration (Supplementary Fig. 13). The lipid in the aquatic phase of cytoplasm (lipids that are not in lipid droplets) would be composed of membrane lipids and are better represented by DOPC. Alternatively, one can perform multi-component NoRI using appropriate Raman bands to quantify different types of lipids as separate components, as saturated lipids, unsaturated lipids, and cholesterol^{2,23,26–28}. Even for the membrane lipids, enrichment of different types of lipids may cause the sample lipidome spectrum deviate from the reference spectrum of DOPC^{2,29,30}. In such cases, one can achieve better spectral decomposition by using tissue lipid extract as the calibration standard.

11.3. Pigmented samples

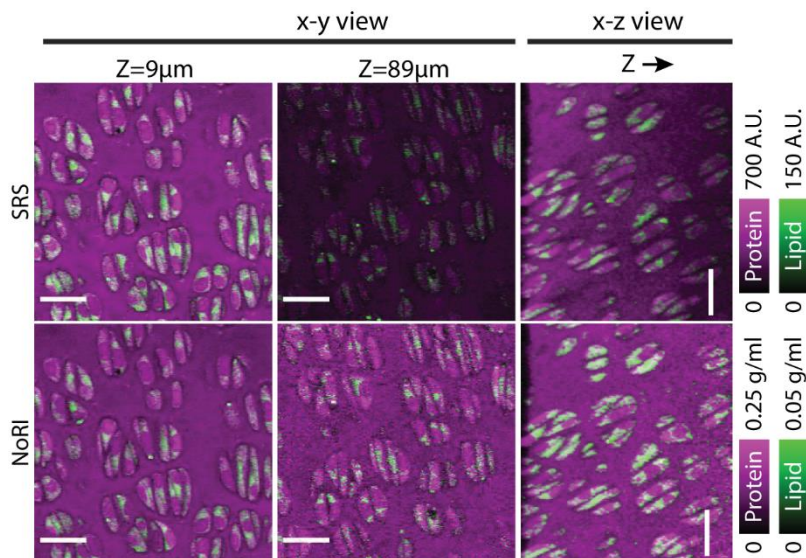
SRS overcomes a large part of the non-Raman background of CARS^{1,31}. The non-Raman backgrounds from cross-phase modulation (XPM) and thermal lensing can be negligible in comparison with the strong Raman signals from the CH₂, CH₃ and H₂O bands (Fig. 1c)^{32–34}. The ratio of signal to background can decrease with depth in thick or highly scattering samples, when the sample configuration requires low NA collection optics, or when imaging weak Raman bands in the fingerprint region or Raman probes at low concentration. In such applications, it is the standard approach to subtract the non-Raman signal from Raman peak images in a way to increase accuracy³⁵. These improvements can also be employed in NoRI. Since the images in the CH₃, CH₂ and H₂O Raman bands are much brighter than the non-Raman background, we decided that it is unnecessary to subtract the non-resonant image when measuring unpigmented samples (Supplementary Fig. 17).



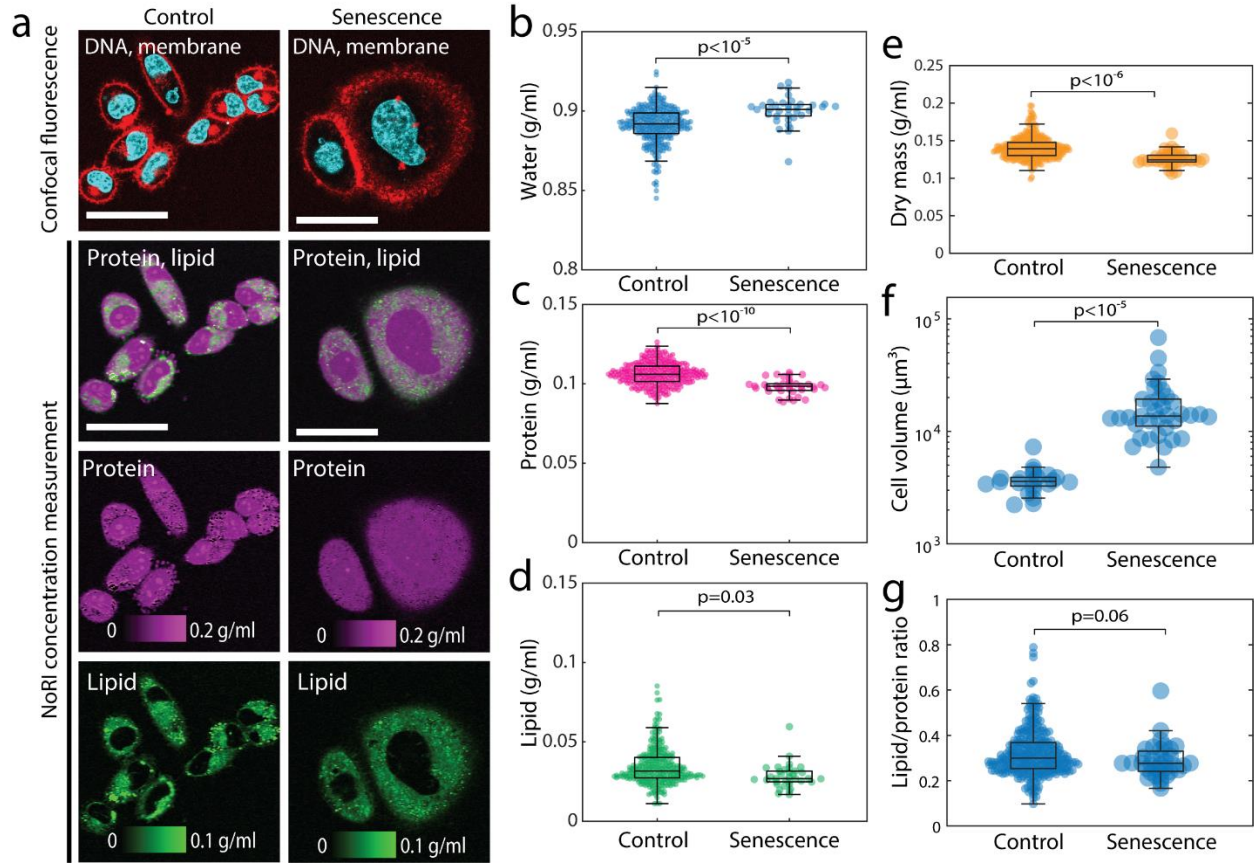
Supplementary Figure 17. Non-Raman background in various tissue samples and blood. (a) Non-Raman signal (acquired at 2125 cm⁻¹) is negligible compared to the SRS signals in the CH₃, CH₂ and H₂O bands in fixed mouse kidney, liver and brain, but it is large in red blood cells. (b) Quantification of SRS intensity and non-Raman signal intensity from images in (a). Photo current is converted to voltage using a 50 Ω

On the other hand, pigments such as hemoglobin, melanin, and lipofuscin can generate two-photon absorption (TPA). Unlike XPM and thermal lensing effect, non-Raman signals from TPA can generate large signals (red blood cells in Supplementary Fig. 17) but these can be subtracted as well due to their flat spectrum³⁴. In practice, we removed red blood cells from samples by perfusing the tissue with saline, and bleached melanin with depigmenting buffer (hydrogen peroxide and formamide) as needed to eliminate TPA instead of computationally subtracting them. Even when saline perfusion is imperfect, the presence of red blood cells does not interfere with the NoRI measurements of the surrounding tissue. Liver may contain bile pigments such as bilirubin and biliverdin. However, we find that a healthy murine liver tissue from 3 month old mouse showed low level TPA under our imaging condition using wavelengths of 770-805 nm and 1045 nm. This is consistent with the absorption spectrum of bile that rapidly drops over 700 nm³⁶.

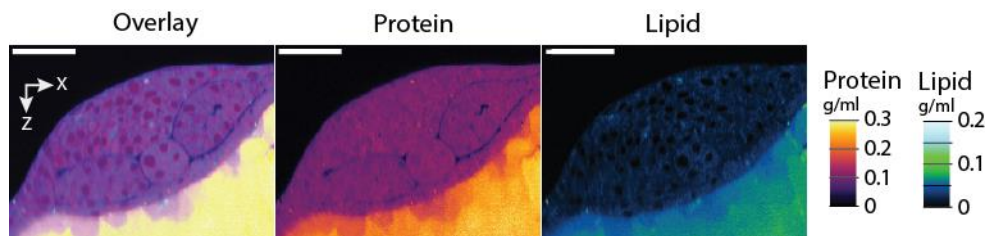
12. Supplementary figures



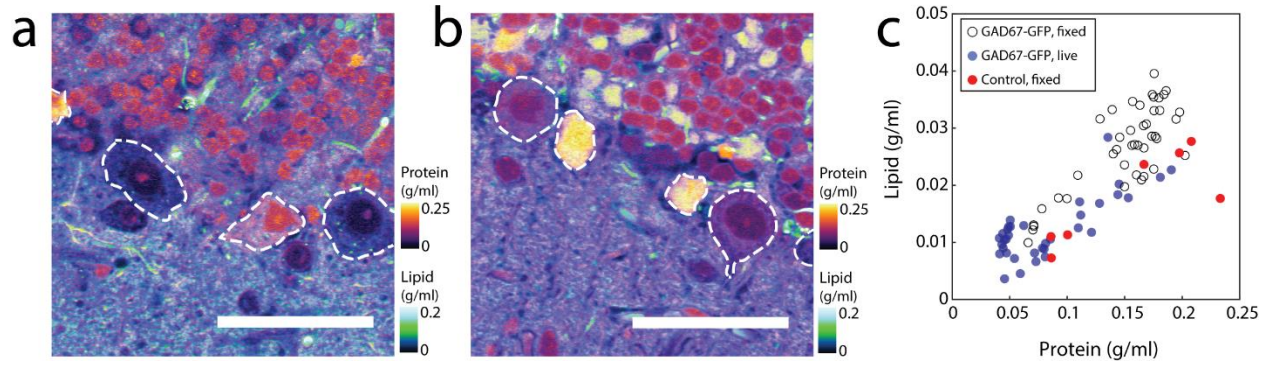
Supplementary Figure 18. Protein and lipid distribution image of live mouse cartilage tissue before and after NoRI normalization. Signal intensity diminishes with imaging depth. Scale bar, 20 μm . NoRI normalization removes the effect of light scattering and enables accurate measurement of protein and lipid concentration throughout tissue volume.



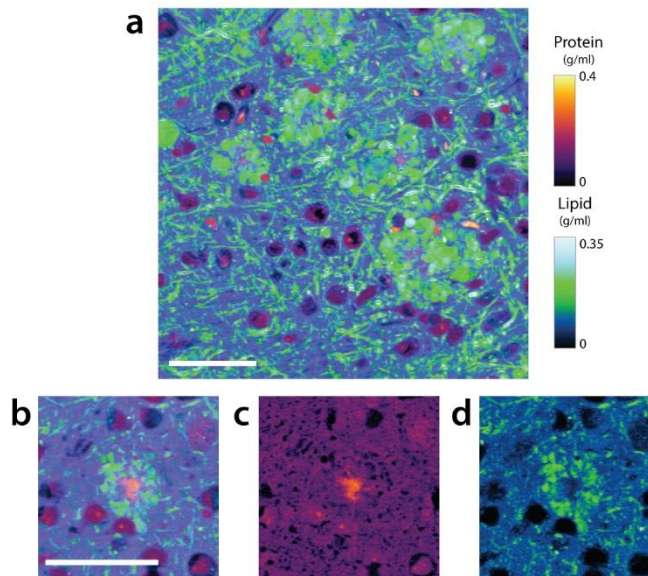
Supplementary Figure 19. Cytoplasm dilution and hypertrophy of senescent A7 cells. (a) Representative images of proliferating and senescent live A7 cells. Senescence is induced by 48 hour doxorubicin treatment. Scale bar, 50 μm . (b-e) Senescent A7 cells have lower protein, lipid, and dry mass concentration and higher water concentration compared to proliferating cells. (Control N=286, mean and standard deviation are water 0.891 ± 0.011 g/ml, protein 0.106 ± 0.007 g/ml, lipid 0.035 ± 0.012 g/ml, dry mass 0.141 ± 0.015 g/ml. Senescence N=35, mean and standard deviation are water 0.900 ± 0.009 g/ml, protein 0.098 ± 0.005 g/ml, lipid 0.028 ± 0.008 g/ml, dry mass 0.127 ± 0.010 g/ml.) (f) Cell volume increase in senescent cells. Mean cell volume is 3693 ± 1035 fl in control cells and 17289 ± 11893 fl in senescent cells. ($p < 0.001$) Senescent cell volume is measured from a membrane localized fluorescence marker (N=36). The control cell volume is measured from 3D segmentation of NoRI dry mass concentration images (N=22). (g) Ratio of lipid mass to protein mass in single cells is 0.32 ± 0.10 in control A7 cells and 0.29 ± 0.08 in senescent A7 cells. ($p = 0.065$)



Supplementary Figure 20. NoRI image of live zebrafish embryo at the 6-somite stage. Scale bar, 50 μm . The protein and lipid concentrations at this stage did not vary much with different embryonic cell types. As expected, yolk granules are packed with proteins and lipids. Individual yolk granules could be recognized adjacent to the embryo as they had lower protein and lipid concentrations, their stores presumably having been partially depleted in the developmental process.



Supplementary Figure 21 (a) A representative NoRI image of live Purkinje cells (outlined) in brain slice from a GAD67-GFP expressing mouse. Scale bar 50 μm . (b) A representative NoRI image of fixed Purkinje cells (outlined) from a mouse that does not express GAD67-GFP (GDF15-KO strain). Scale bar 50 μm . (c) Protein and lipid concentration of Purkinje cells. Concentration variation is reproduced in both live and fixed cells and in GFP expressing and non-expressing cells. Fixed GFP expressing, N=38. Live GFP expressing, N=35. Fixed non-expressing control, N=7.



Supplementary Figure 22. NoRI protein and lipid concentration images of 5xFAD mouse brain tissue. (a) Protein and lipid concentration images of a 5xFAD mouse brain tissue. (b) Detailed view of a senile plaque in 5xFAD mouse shows a core of protein aggregates surrounded by a lipid-rich corona. Scale bars, 50 μm . (c) Protein only view (b). (d) Lipid only view of (b).

13. Supplementary references

1. Freudiger, C. W. *et al.* Label-free biomedical imaging with high sensitivity by stimulated Raman scattering microscopy. *Science* (80-.). **322**, 1857–1861 (2008).
2. Fu, D., Holtom, G., Freudiger, C., Zhang, X. & Xie, X. S. Hyperspectral imaging with stimulated raman scattering by chirped femtosecond lasers. *J. Phys. Chem. B* **117**, 4634–4640 (2013).
3. Silva, W. R., Graefe, C. T. & Frontiera, R. R. Towards Label-Free-Resolution Microscopy. *ACS Photonics* **3**, 79–86 (2016).
4. Zipfel, W. R., Williams, R. M. & Webb, W. W. Nonlinear magic: Multiphoton microscopy in the biosciences. *Nat. Biotechnol.* **21**, 1369–1377 (2003).
5. Liu, X. Computationally Enhanced Quantitative Phase Microscopy. (2020).
6. Lachmann, P. J. *The Plasma Proteins: Structure, Function, and Genetic Control.* Frank W. Putnam . *The Quarterly Review of Biology* vol. 61 (Academic Press, 1986).
7. Greenwood, A. I., Tristram-Nagle, S. & Nagle, J. F. Partial molecular volumes of lipids and cholesterol. *Chem. Phys. Lipids* **143**, 1–10 (2006).
8. Wells, R. D. & Larson, J. E. Buoyant density studies on natural and synthetic deoxyribonucleic acids in neutral and alkaline solutions. *J. Biol. Chem.* **247**, 3405–3409 (1972).
9. Trepats, X. *et al.* Physical forces during collective cell migration. *Nat. Phys.* **5**, (2009).
10. Zhao, H., Brown, P. H. & Schuck, P. On the distribution of protein refractive index increments. *Biophys. J.* **100**, 2309–2317 (2011).
11. Arganda-Carreras, I. *et al.* Trainable Weka Segmentation: a machine learning tool for microscopy pixel classification. *Bioinformatics* **33**, 2424–2426 (2017).
12. Püspöki, Z., Storath, M., Sage, D. & Unser, M. Transforms and operators for directional bioimage analysis: A survey. *Adv. Anat. Embryol. Cell Biol.* **219**, 69–93 (2016).
13. Hoffmann, H. violin.m - Simple violin plot using matlab default kernel density estimation. INRES (University of Bonn), Katzenburgweg 5, 53115 Germany, hhoffmann@uni-bonn.de.
14. Lu, F.-K. *et al.* Multicolor stimulated Raman scattering microscopy. *Mol. Phys.* **110**, 1927–1932 (2012).
15. Wilson, B. C., Patterson, M. S., Flock, S. T. & Moulton, J. D. The Optical Absorption and Scattering Properties of Tissues in the Visible and Near-Infrared Wavelength Range. in *Light in Biology and Medicine* (eds. R.H., D., J., M. & F., D.) vol. 4 45–52 (Springer, 1988).
16. Jacques, S. L. Optical properties of biological tissues: a review. *Phys. Med. Biol.* **58**, R37 (2013).
17. Hill, A. H., Manifold, B. & Fu, D. Tissue imaging depth limit of stimulated Raman scattering microscopy. *Biomed. Opt. Express* **11**, 762 (2020).
18. Fu, D. *et al.* Two-color excited-state absorption imaging of melanins. in *Photonic Therapeutics and Diagnostics III* (eds. Kollias, N. *et al.*) vol. 6424 642402 (International Society for Optics and Photonics, 2007).

19. Fu, D. *et al.* High-resolution in vivo imaging of blood vessels without labeling. *Opt. Lett.* **32**, 2641 (2007).
20. Alberts B, Johnson A, Lewis J, *et al.* The Chemical Components of a Cell. in *Molecular Biology of the Cell. 5th edition.* 63 (Garland Science, 2008).
21. Huizinga, A., Bot, A. C. C., de Mul, F. F. M., Vrensen, G. F. J. M. & Greve, J. Local variation in absolute water content of human and rabbit eye lenses measured by Raman microspectroscopy. *Exp. Eye Res.* **48**, 487–496 (1989).
22. Liao, C. S. *et al.* Microsecond scale vibrational spectroscopic imaging by multiplex stimulated Raman scattering microscopy. *Light Sci. Appl.* **4**, 1–9 (2015).
23. Freudiger, C. W. *et al.* Highly specific label-free molecular imaging with spectrally tailored excitation-stimulated Raman scattering (STE-SRS) microscopy. *Nat. Photonics* **5**, 103–109 (2011).
24. Lu, F.-K. *et al.* Label-free DNA imaging in vivo with stimulated Raman scattering microscopy. *Proc. Natl. Acad. Sci.* **112**, 11624–11629 (2015).
25. King, J. L. & Jukes, T. H. Non-Darwinian evolution. *Science (80-.)*. **164**, 788–98 (1969).
26. Yan, S. *et al.* Hyperspectral Stimulated Raman Scattering Microscopy Unravels Aberrant Accumulation of Saturated Fat in Human Liver Cancer. *Anal. Chem.* **90**, 6362–6366 (2018).
27. Li, J. *et al.* Lipid desaturation is a metabolic marker and therapeutic target of ovarian cancer stem cells. *Cell Stem Cell* **20**, 303–314 (2017).
28. Fu, D. *et al.* In vivo metabolic fingerprinting of neutral lipids with hyperspectral stimulated raman scattering microscopy. *J. Am. Chem. Soc.* **136**, 8820–8828 (2014).
29. Christie, W. W. Rapid separation and quantification of lipid classes by high performance liquid chromatography and mass (light-scattering) detection. *J. Lipid Res.* (1985).
30. Jamieson, L. E., Li, A., Faulds, K. & Graham, D. Ratiometric analysis using Raman spectroscopy as a powerful predictor of structural properties of fatty acids. *R. Soc. Open Sci.* **5**, (2018).
31. Min, W., Freudiger, C. W., Lu, S. & Xie, X. S. Coherent Nonlinear Optical Imaging: Beyond Fluorescence Microscopy. *Annu. Rev. Phys. Chem* **62**, 507–530 (2011).
32. Stolow, A., Pegoraro, A. F., Popov, K. I. & Ramunno, L. Image formation in CARS and SRS: effect of an inhomogeneous nonresonant background medium. *Opt. Lett. Vol. 37, Issue 4, pp. 473-475* **37**, 473–475 (2012).
33. Berto, P., Andresen, E. R. & Rigneault, H. H. Background-free stimulated raman spectroscopy and microscopy. *Phys. Rev. Lett.* **112**, 53905 (2014).
34. Xiong, H. *et al.* Background-free imaging of chemical bonds by a simple and robust frequency-modulated stimulated Raman scattering microscopy. *Opt. Express* **28**, 15663 (2020).
35. Shi, L. *et al.* Optical imaging of metabolic dynamics in animals. *Nat. Commun.* **9**, (2018).
36. Nachabé, R. *et al.* Effect of bile absorption coefficients on the estimation of liver tissue optical properties and related implications in discriminating healthy and tumorous samples. *Biomed. Opt. Express* **2**, 600 (2011).